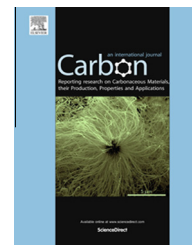


Available at www.sciencedirect.com

ScienceDirect

journal homepage: www.elsevier.com/locate/carbon

Graphene nanoribbons formed by a sonochemical graphene unzipping using flavin mononucleotide as a template

Woojin Yoon^a, Yonggeun Lee^a, Hongje Jang^a, Myungsu Jang^a, Jin Sung Kim^b, Hee Sung Lee^b, Seongil Im^b, Doo Wan Boo^a, Jiwoong Park^c, Sang-Yong Ju^{a,*}

^a Department of Chemistry, Yonsei University, Seoul 120-749, Republic of Korea

^b Department of Physics, Yonsei University, Seoul 120-749, Republic of Korea

^c Department of Chemistry and Chemical Biology, Cornell University, Ithaca, NY 14853, USA

ARTICLE INFO

Article history:

Received 11 August 2014

Accepted 30 September 2014

Available online 7 October 2014

ABSTRACT

When the width of a graphene nanoribbon (GNR) is only a few nanometers, it possesses semiconducting properties that enable various high-end electronic applications. In this study, we report that the dense and stable dispersion of a natural graphite formed using flavin mononucleotide (FMN) as a surfactant produces GNRs as small as 10 nm in width. High-resolution transmission electron microscopy reveals GNRs with various widths, along with a graphene flake containing straight-edged GNRs and cuts, depending on substrate treatments. Such nanoribbon formation originates from sonochemical graphene unzipping with a one-dimensional FMN supramolecular ribbon as a template. Raman spectroscopy demonstrates the universal intensity ratio of D over D' bands near 4, supporting formation of continuous edge defect. Thermal annealing enhances the optical contrast and van der Waals interactions of the graphene film, resulting in increased conductivity compared to the as-prepared graphene film, which is also better than that of reduced graphene oxide.

© 2014 Elsevier Ltd. All rights reserved.

1. Introduction

Graphene nanoribbon (GNR), a narrow strip of graphene, has attracted attention because of its novel optical [1], electrical [2], and spin properties [3]. GNRs with a bandgap greater than 0.3 eV can be utilized as transistors with a high current on/off ratio up to 10^7 [4]. The edge configurations of GNR (i.e., zigzag and armchair) [3] also determine its electronic properties, where the armchair configuration of graphene edges displays a bandgap inversely

proportional to GNR width, and a zigzag arrangement acts as a spin valve under a magnetic field [5,6].

GNR has been prepared using various methods including metal-assisted chemical unzipping of graphene [7–9], unzipping of graphite [4] and carbon nanotubes [10–12], e-beam lithography [13], and bottom-up synthesis from precursor [14]. Dai and coworkers [4] produced GNRs of various widths by sonicating expandable graphite in the presence of a rigid-rod conductive polymer as a surfactant. Although the transistor employing GNRs below 10 nm in width displays

* Corresponding author.

E-mail address: syju@yonsei.ac.kr (S.-Y. Ju).

<http://dx.doi.org/10.1016/j.carbon.2014.09.097>

0008-6223/© 2014 Elsevier Ltd. All rights reserved.

excellent current on/off ratio [4], the random coil structures of the polymer on graphene seem to produce GNRs with various widths. GNR with atomically-precise width was attained by metal surface-assisted polymerization of aromatic precursors [14]. This method demonstrated GNRs with monodisperse width, while their length (<100 nm) was shorter than that required for electronic applications. The reliable large-scale production of GNRs smaller than 10 nm in width remains a significant challenge.

Among various preparation methods, dispersion methodology can obtain GNRs in large quantities. In order to prepare GNRs with a surfactant, dispersion methodology needs (i) to overcome strong van der Waals (vdW) interactions between graphene sheets (i.e., 31 meV/atom) [15], and (ii) directional unzipping of graphene. In addition, compared to acid-assisted unzipping, the noncovalent method using surfactant is expected to preserve GNR electrical properties. One-dimensional assembly of surfactant on graphene would be the ideal platform to attain such graphene unzipping.

Here, we demonstrate that flavin mononucleotide (FMN) and its analogue disperse natural graphite into graphene nanoribbons as small as 10-nm wide. FMN serves as both a surfactant and one dimensional template to induce graphene unzipping. High-resolution transmission electron microscopy (HRTEM) demonstrated that the dense dispersion contains GNRs with various widths, unlike graphene flakes irregularly cracked by sodium dodecyl sulfate (SDS). Raman study supported that edge of GNR acts like defects, and showed large and uniform intensity of D over D' bands, revealing that the lined defect density is one per few nanometer, supporting HRTEM result. The resulting graphene film exhibited good electrical properties in film. These results provide a valuable tool for shaping GNR using self-assembled surfactant, and route to a solution-processed graphene for flexible electronics and membrane applications.

2. Experimental

2.1. Materials and instrumentations

FMN (73–79%, Cat#: 77623-50G-F) was purchased from Sigma Aldrich. SDS (95%, Cat#: I0352) was obtained from TCI. Spectroscopic-grade deionized water was obtained from Alfa Aesar. 3-Aminopropyl dimethyl ethoxy silane (APDMES, 97%, Lot#: 1216392) was obtained from abcr GmbH (Germany). FC12 was synthesized according to previous literature [16]. Natural graphite flakes were kindly donated by Asbury Graphite (+50 mesh, 3061 grade, USA). All other solvents were spectroscopic grade. UV–vis absorption spectra were measured with a Cary 5000 spectrometer using a cuvette with a path length of 10 mm. Transmittance of graphene film on a glass substrate was obtained by using 550 nm bandpass filter. Optical images were obtained using an upright microscope (BX51, Olympus) equipped with a CMOS camera (1280 × 1024 pixels, 3.6 × 3.6 μm²/pixel, DCC1645C, Thorlabs). Four-point probe measurements were conducted with a FPP-40K (Bega Technologies Co., Korea). Error bars were obtained by averaging sheet resistance values from five different locations.

2.2. Dispersion of graphene flakes using surfactants

2.2.1. FMN-based dispersion

Two grams of natural graphite flakes and 0.40 g of FMN were added to 20 mL of H₂O. The resulting mixture was cup-horn sonicated for 2 h at 450 W. The resulting dark dispersion was ultra-centrifuged in SW41Ti rotor (Beckman coulter) with an average 80,000g centrifugal force at 22 °C for 1 h, and then the supernatant (upper 80%) was carefully collected for measurement.

2.2.2. FC12-based dispersion

Similarly, an organic dispersion of natural graphite was obtained using FC12 as a surfactant. Briefly, 2.5 mg of natural graphite was mixed with 10 mg of FC12 in 10 mL of xylene. After probe sonication of the mixture for 4 h at 300 W, the sample was centrifuged for 3 h at 20,000g, and 80% of the supernatant was collected for TEM measurement.

2.2.3. SDS-based dispersion

Similar to the FMN dispersion protocol, 2.00 g of natural graphite flakes and 0.40 g of SDS were added to 20 mL of H₂O. The sonication and centrifugation steps were the same as the FMN-based dispersion.

2.3. Preparation of amine-terminated substrate on prepatterned SiO₂/Si substrates for AFM/optical/Raman measurements

Si wafers covered with a 285-nm-thick thermal oxide layer were patterned by photolithography using a contact mask aligner. Prepatterned markers were obtained by etching a SiO₂ using a reactive ion etcher (RIE). Cleaning of the patterned substrates were performed (i) by immersing them in acetone to remove a photoresist, and (ii) by sonicating using a bath-sonicator (Branson 1510, max. power: 80 W) for 10 min. Any organic residues of the patterned substrate pieces were further removed by immersing them in piranha solution (H₂SO₄:H₂O₂ = 7:3) for 20 min, and subsequent washing by flow of Milli-Q quality water for 5 min. The substrates were dried with a N₂ stream, and were further dried in a vacuum oven at 110 °C for 1 h. In order to promote adhesion of hydrophobic graphene flakes, the dried substrates were functionalized with an amine group by placing concentrated APDMES liquid in between the substrates for 10 min. APDMES promotes the adhesion of graphene on the substrate by substantial amine interactions with the graphene surface [17], and the dimethyl group of APDMES prevents crosslinking and provides a clean, flat surface, as compared to amino propyl triethoxy silane (see Fig. S1A and B of Supporting Information (SI)).

2.4. Atomic force microscopy (AFM) measurement

The sample was prepared by depositing 150 μL FMN-assisted graphene dispersion on the amine-terminated Si substrate and incubating for 10 h, according to previous literature [21,18]. The remaining solution was removed by wicking with Kimwipes. Several repetitions of water incubation (15 min each) and consecutive wicking steps were performed to

remove extra FMN. In order to remove any remaining water, careful overnight drying of the sample was conducted prior to AFM. AFM measurements were conducted primarily using a commercial AFM (Veeco Nanoscope IIIa equipped with Bruker multimode head), and AFM equipped with an inverted microscope (XE-bio, Park systems). Al-coated silicon AFM probes (HQ:NSC15-AL BS, tip curvature = 8 nm, force constant = 40 N/m, μ masch) were utilized throughout this study. All topography images were obtained in a tapping mode, and 512×512 -pixel images were acquired over an $80\text{-}\mu\text{m}^2$ area. Flattening of the acquired surface morphology was conducted using third-order polynomial regression with speckle removal. Height distribution was obtained by analyzing a total of 50 graphene flakes.

2.5. Contrast measurement

Contrast of graphene flakes was measured using an upright microscope (BX51, Olympus) with a LED light source (MCWHL2-C1, Thorlabs). A bandpass filter for green light (FWHM = 10 nm, FB550-10, Thorlabs) was employed to the excitation to obtain the quantitative contrast measurement [19,20]. Contrast images were recorded using a charge-coupled device (CCD) ($6.45\ \mu\text{m}^2/\text{pixel}$, 1392×1040 , CoolSNAP HQ², Photometrics) for 0.03 s of acquisition with 0.08 mW 500 nm excitation light. The 106 graphene flakes were analyzed to obtain lateral length by Image J, discarding values smaller than 8 μm .

2.6. HRTEM measurements

TEM specimens were prepared as described previously [21]. Copper TEM grids covered with an ultra-thin carbon support film on a lacey carbon support (LC200-Cu (Lot#: 110727), 200 mesh, Ted Pella) were used. To facilitate sample deposition, grids were exposed to a high intensity UV light for 3 min [22]. Oxygen plasma treatment for 5 s was applied to obtain a preferential deposition of GNRs. The FMN-graphene sample was diluted (100 \times) and a 5 μL portion was dropcast on the TEM grid. After 3 min of incubation, excess sample was carefully wicked off the grid using a filter paper, and the sample was dried overnight. Transmission electron microscopy (TEM) measurements were conducted using either a JEOL 2100-F with a 200-kV acceleration voltage or FEI Tecnai F20.

2.7. Raman/widefield Raman measurements

The Raman setup was built according to previous literature [23] with exception of an BX51 upright microscope (Olympus) as a platform. A high power, diode-pumped solid state (DPSS) laser (532 nm) was used as an excitation source [21]. The beam was passed through a laser bandpass filter and linearly polarized through a polarizing cube, and the beam size was adjusted with a beam expander. A large collimated illumination beam (50–100 μm in diameter) was obtained by focusing the laser at the back focal plane of the objective lens (50 \times , MPlan (N.A. = 0.75) or 20 \times , UPLanFL (N.A. = 0.50), Olympus) using a convex lens (achromat, $f = 200$ mm, Thorlabs). The power delivered to the sample was orders of magnitude

greater than that used by the micro Raman technique (up to tens of mW for widefield Raman imaging on graphene vs. 0.1 mW for micro Raman on graphene), but the power per unit remained low ($0.1\ \text{mW}/\mu\text{m}^2$ for both techniques).

The collimated light illuminated the sample and the scattered light was collected via the same objective lens, passing through a dichroic beam splitter and long bandpass filter to eliminate the elastically-scattered light. The selection of specific Raman bands was performed by single bandpass (FWHM = 10 nm, Thorlabs) before the light entered the image spectrometer (Triax320, Horiba). The imaging spectrometer contained a turret with an interchangeable 1800 g/mm, 500-nm blaze grating (spectral mode). Images were recorded using a CCD camera (Symphony, $26\ \mu\text{m}/\text{pixel}$, 1024×256 , Horiba Jobin-Yvon).

2.8. Graphene film preparation and thermal annealing for XPS/optical/electrical measurements

Samples were obtained from filtrations of the dispersed samples using a solvent-dissolvable filter [24]; the dispersed sample was first filtered with a mixed cellulose ester membrane (diameter: 2.5 cm, pore size: 0.1 μm , Lot#: 00728200, Advantec), and the filtrate was washed with copious amounts of water. While the membrane was still wet, the graphene-containing membrane was firmly pressed between piranha-cleaned soda-lime slide glass (Cat#: 1000412, Marienfeld, Germany). After fixing the graphene side to the slide glass, the membrane was gently dissolved with acetone for 2 days. Thermal annealing for contrast, AFM, and electrical measurement was performed by placing the sample in a clean chemical vapor deposition chamber at 300 $^\circ\text{C}$ for 2 h under either an Ar (for electrical measurement) or air (for XPS, transmittance) atmosphere.

2.9. X-ray photoelectron spectrometer (XPS) measurement

XPS data was acquired by K-alpha (Thermo Scientific, U.K.). A monochromatic X-ray source (Al K_{α} line: 1486.6 eV), whose beam size is $\sim 400\ \mu\text{m}$ was used with power of 12 kV and 3 mA, and a base pressure of 1.9×10^{-9} mbar. Survey scans were acquired with a 100 eV pass energy at resolution of 1 eV, with respect to the C1s peak at 284.8 eV. Detailed scans were obtained at a 20 eV pass energy with a resolution of 0.05 eV. The acquired spectra were baseline-subtracted using the Shirley baseline, and the C1s spectra was deconvoluted with Voigt shapes (Gaussian:Lorentzian = 7:3) [25,26].

2.10. Device fabrication and electrical measurement

Graphene film with the desired transmittance was transferred to a 285-nm thick SiO_2/Si substrate (Lot#: 7400383–603-Z, degenerately *p*-doped, resistivity = 1–10 $\Omega\text{-cm}$, Shinetsu, Japan). A field effect transistor (FET) device was fabricated by evaporating 100-nm-thick Au electrode via thermal evaporation method. Using a backgate geometry, current-voltage (*I*-*V*) characteristics were measured using a semiconductor parameter analyzer (HP 4155C, Agilent Technologies) under ambient conditions.

3. Results and discussion

3.1. Dispersion and characterization of FMN-dispersed few-layered graphene

FMN (dotted box of Fig. 1A) is a phosphate analogue of vitamin B₂ (riboflavin) and consists of three aromatic rings (i.e., isoalloxazine) along with an anionic phosphate tail group. The aromatic isoalloxazine moiety has a profound binding affinity (~ 2 eV) to graphene sidewalls as calculated by the density functional theory [27]. Such a strong binding affinity enables the dispersion of single-walled carbon nanotubes (SWNTs) [22,28], and boron nitride nanotubes [28] in aqueous [22,28], and organic solvents [16]. For this, the supramolecular assembly of FMN plays an important role for dispersing and sorting SWNT chiralities [21,22]. Hydrophilic ribityl phosphate tail groups provide ionic repulsion between the dispersed graphene layers. A pictorial illustration of such graphene dispersion is shown in Fig. 1A.

A dispersion of graphene was obtained using a sonochemical method using FMN. Briefly, a mixture of two grams natural graphite and 0.4 g FMN was cup-horn sonicated in 20 mL of water at 300 W for 2 h. The subsequent dispersion was centrifuged at 80,000g for 1 h. The inset of Fig. 1B shows a photograph of the graphene dispersion, showing a dense black color without any flocculation of graphene for at least one year. Fig. 1B displays the subsequent UV–vis absorption spectrum. While the FMN absorption tail ends at 550 nm, the absorbance from 600 to 800 nm slightly decreases due to the linear relationship between the excitation energy and the density of state of graphene near the Dirac cone, along with minor contribution from scattering background, whose intensity is proportional to wavelength λ^{-4} [29]. The measured absorption at 600 nm was ~ 0.78 . Since graphene exhibits 97.7% transmittance (T) per layer over the visible range due to the fine structure constant α of one-atom thick graphene [30], α is utilized to calculate the graphene dispersibility. Assuming there is no scattering contribution of the graphene flake, since the absorption (A) can be expressed as $A = -\log_{10} T$, ~ 78 layers of single-layered graphene lie in a 1 cm beam path. The modification of the centrifugation condition (10,000g for 1 h) resulted in enhanced graphene dispersibility up to 0.24 mg/mL after removing the surfactant by annealing

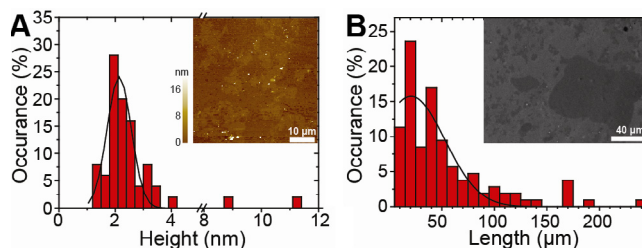


Fig. 2 – Height and size distributions of graphene flakes on a Si substrate after 300 °C thermal annealing in Ar. (A) Histogram of the height distribution of the graphene flakes. The inset illustrates an AFM image having few-layered graphene flakes. (B) Histogram of the graphene lateral length obtained by taking the square root of the measured size. Inset: OM image for size distribution measurement. (A colour version of this figure can be viewed online.)

at 300 °C. This value is approximately 20 times greater than that of N-methyl pyrrolidone (NMP)-dispersed graphene [31]. With similar protocol (see Section 2), FC12 (10-dodecyl isoalloxazine, dotted box of Fig. 1A) was able to disperse graphene in xylene in a lesser extent, as shown in Fig. 1B.

The height and size distributions of the resulting graphene flake by FMN after 300 °C annealing were further examined by atomic force microscopy (AFM) and optical microscopy (OM), respectively. Samples were prepared by dropping the dispersion on an amine-terminated, 285-nm-thick SiO₂/Si substrate (see Section 2). 300 °C annealing is necessary both to remove extra surfactants, and to enhance the interaction between graphene layers, by observing reduced graphene thickness and increased contrast value (see SI for the detailed explanation and Fig. S2). The inset of Fig. 2A displays an AFM image of the graphene flakes, where displays uniform height over various graphene flakes. As shown in Fig. 2A, the most probable height is 2.1 nm, showing a Gaussian distribution height profile with its full width at half maximum (FWHM) of 1 nm. Graphene flakes with a height greater than 8 nm were observed with a frequency less than 6%. This suggested that most graphene flakes consisted of graphene with less than six layers. Fig. 2B displays the lateral length distribution of the graphene obtained from 106 flakes, by taking the square

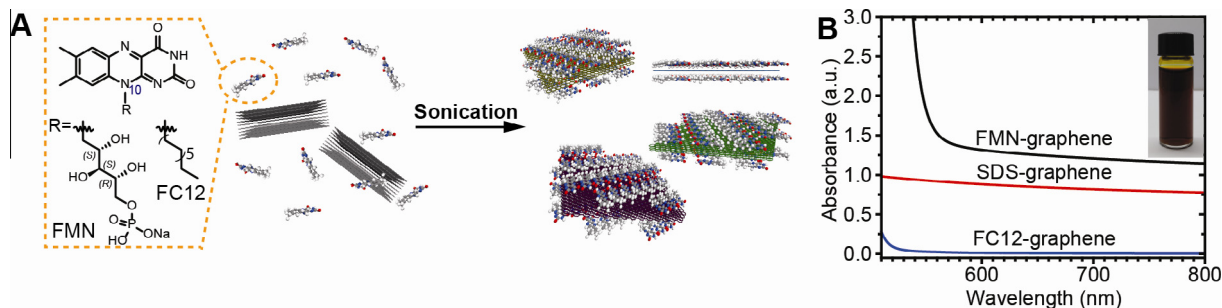


Fig. 1 – Schematic illustration of graphene dispersion with FMN and FC12 using a sonochemical method. (A) Pictorial illustration of FMN-assisted dispersion of graphene, where lumiflavin (10-methyl isoalloxazine, circled) was used instead of FMN for visual clarity. The dotted box illustrates the chemical structure of FMN, and (B) UV–vis absorption spectra of FMN-, sodium dodecyl sulfate (SDS)-dispersed graphene in water, and 10-dodecyl isoalloxazine (FC12)-dispersed graphene in xylene. Inset: photograph of the aqueous dispersion of FMN-graphene. (A colour version of this figure can be viewed online.)

root of the measured size. The lateral length showed its maximum at 21 μm , with a 76- μm FWHM of the Gaussian profile. This value was 10 times less than that (i.e., average flake size: 300 μm) of the as-supplied natural graphite, suggesting that the chemical exfoliation is effective.

3.2. Graphene flakes and graphene nanoribbons observed by HRTEM

Fig. 3A through E exhibits several HRTEM images of large graphene flakes with lateral lengths ranging 100 nm to micrometer dispersed by FMN. The graphene flake deposited on a UV-treated holey lacey carbon grid exhibited irregular

outer shapes stacked on top of each other. Surprisingly, upon closer inspection (Fig. 3A), the graphene flakes revealed many randomly-oriented, straight cuts extending up to a few hundreds of nanometers (indicated by red arrows). More clear image can be observed in a few-layered graphene region (Fig. 3B), while illustrates that the stacked graphenes possess randomly-oriented line cuts having approximate 1-nm width. Some cuts (indicated by the yellow double arrows) of the graphene are parallel, forming clearly visible graphene nanoribbons of 15.1- and 31.6-nm widths with lengths greater than 250 nm. Certain GNRs have widths as small as 5.3 nm. Graphene cuts, indicated by the green arrow, were spread and rolled in the middle part of the cut. In order to obtain the density of

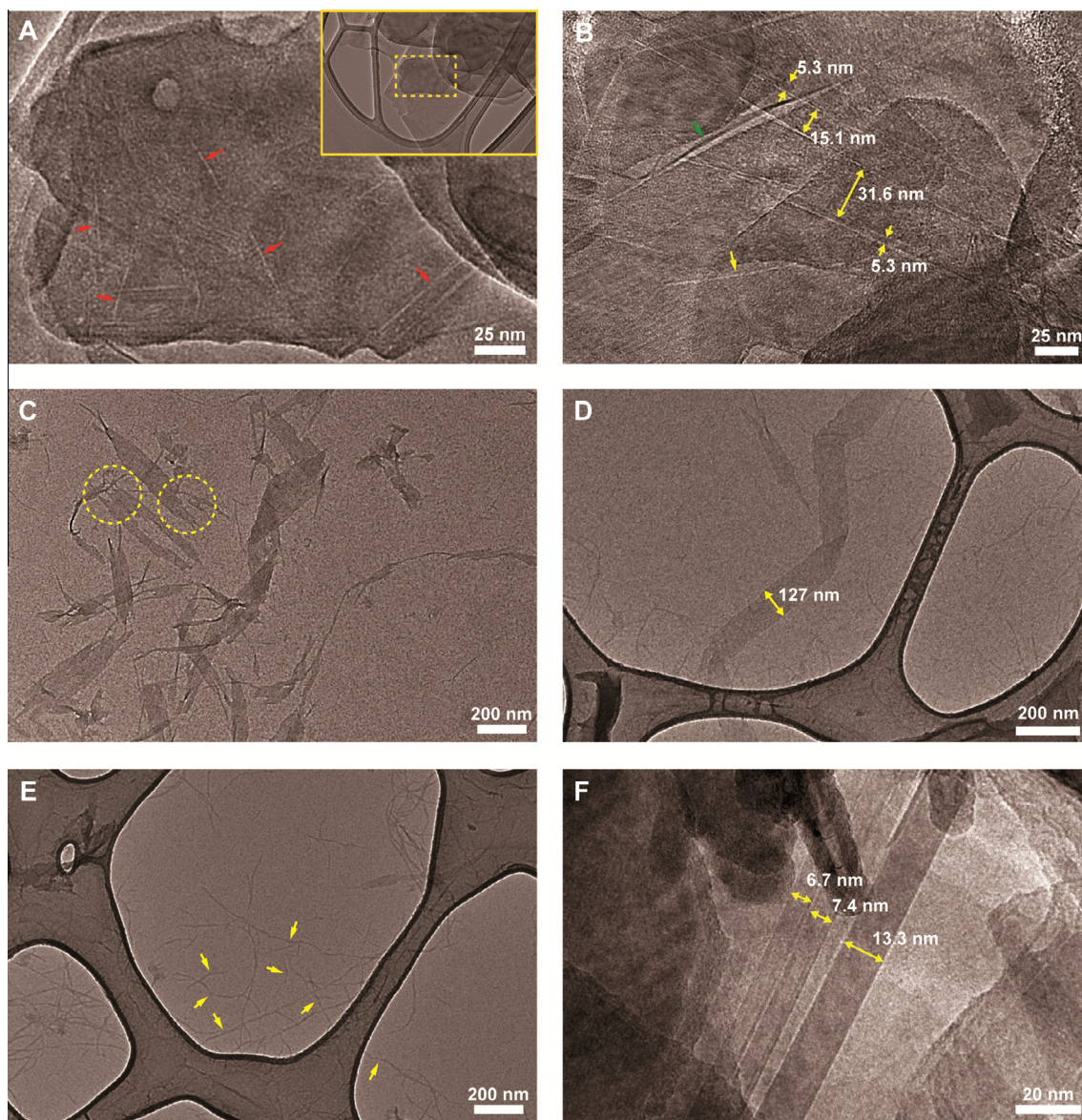


Fig. 3 – HRTEM images of graphene flake and nanoribbons, dispersed by flavin derivatives. (A and B) HRTEM images of graphene flakes, deposited on a UV-treated holey lacey carbon grid. (A) High magnification image of flake shown in inset. Linear cuts (red arrows) are visible. (B) Image of various nanoribbons (yellow arrows) with different widths and nanocut (green arrow) on a flake. (C–E) HRTEM images of GNRs deposited on a O_2 plasma-treated holey lacey carbon grid. (C) Images of individual GNRs with various width, torn from graphene flake. Images of (D) folded, and (E) twisted GNRs. (F) HRTEM images of various GNRs prepared by FC12-dispersed graphene. (A colour version of this figure can be viewed online.)

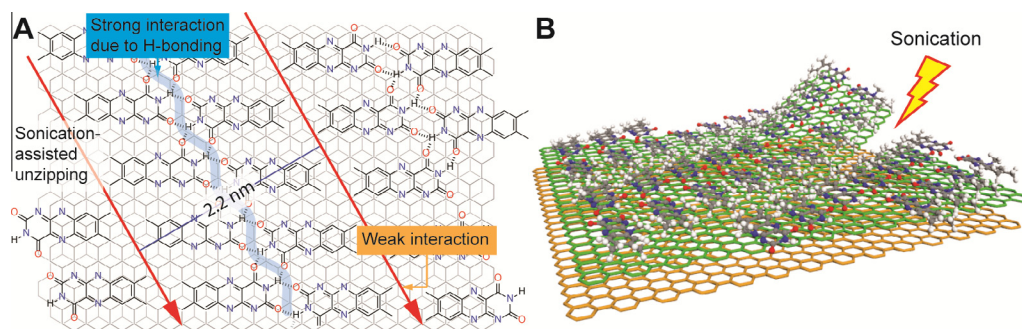


Fig. 4 – Flavin assembly-assisted sonochemical unzipping of graphene into graphene nanoribbon. (A) Self-assembled 1D flavin nanoribbons on graphene, showing strong H-bonding compared to weak vdW interaction between dimethyl tail groups. Unzipping is propagated along the weak interaction line, as shown by straight arrows. (B) Pictorial illustration of graphene unzipping into graphene nanoribbons upon sonication. (A colour version of this figure can be viewed online.)

the cutting in a given area, the cutting lines of Fig. 3B were visualized in Fig. S3 of the SI. The total length of cuts was approximately 1942 nm. Divided by the total area (i.e., 61459 nm²), the value was 0.032 lines/nm, indicating that a line cut occurs every 31 nm. Since every cut serves as two edges, the defect density becomes one every 16 nm. Notice that plane of graphene nanoribbons preferentially adheres to underlying graphene, showing strong vdW interaction. These observations suggest that graphene flake serves as a precursor to produce GNRs with various width.

Isolated graphene nanoribbons (Fig. 3C through E) were preferentially observed by hydrophilic grid, obtained by 5-s oxygen plasma treatment. As shown in Fig. 3C, isolated GNRs originate from nanometer-sized graphene flakes with large aspect ratio. Graphene flakes with many unfinished cuts are readily visible, and GNRs are hanging to such graphene flake. Edge shape of the flake is anisotropic (yellow circles in Fig. 3C): while transverse edges are irregular, longitudinal edges are relatively smooth. Unlike graphene nanoribbons on a flake in Fig. 3A and B, frequent folding (Fig. 3D) and twisting was observed for graphene nanoribbons on a O₂-treated grid. As indicated by yellow arrows in Fig. 3E, average width and length of GNRs were 8.9 and 250 nm, respectively, and GNRs has highly twisted configuration. It is known that since edges of GNR are highly stressed due to the terminal groups such as hydrogen and other functional moieties, and are different from the bulk value of graphene, twisting of GNR is spontaneous and energetically favorable [32,33]. Control experiment exposing similar O₂ treatment on a bare grid does not produces any of such features (Fig. S4 of the SI).

Unzipping graphene into graphene nanoribbon (Fig. 3F) in organic solvent was also obtained by using FC12 [16]. The graphene nanoribbons were clearly isolated, with widths of approximately 6.7, 7.4, and 13.3 nm, and lengths that persist over a few hundreds of nanometers. Overall, the cuts and their edges were quite sharp and smooth. In order to verify whether the sharp cuts and edges originate from other surfactants, natural graphite was dispersed with flexible sodium dodecyl sulfate (SDS), forming micellar structure on graphene (see Method for its dispersion process. Absorption spectrum was shown in Fig. 1B). Similar to the process of FMN-decorated graphene dispersion, HRTEM images were taken

(Fig. S5 of the SI). Only multiple irregular cracks in the graphene flake were observed. Similarly, sodium cholate is known to produce irregular graphene flake [24]. This result suggests that the rigid isoalloxazine moiety is the primary reason for such sonication-assisted sharp unzipping of graphene flakes.

The template effect of one-dimensional organization of the flavin moiety seems to be origin of such GNR formation. Fig. 4 illustrates the schematics of hydrogen-bonding-assisted graphene organization on graphene. Zhang et al. [34] reported that the flavin adenine dinucleotide, an analogue of FMN, is self-assembled into one-dimensional nanoribbon onto a highly ordered pyrolytic graphite (HOPG), as illustrated in Fig. 4A. This FMN ribbon has two interfacing parts: a quadruple hydrogen-bonded (indicated by ribbon) uracil part of the adjacent isoalloxazine and a vdW part (indicated by orange arrows) between dimethyl groups of isoalloxazine. As a result, strong hydrogen bonding having energy of a few kcal/mol fortifies the adsorbed FMN ribbon on graphene, while dimethyl groups of FMN loosely interacts with the adjacent FMN ribbon [35] via vdW interaction. This hydrogen-bonded, one-dimensional structure makes this FMN ribbon robust against external stimuli. Since one FMN ribbon with a width of 2.2 nm (Fig. 4A) serves as a template on the graphene surface, its sonication-assisted unzipping can modulate width of the produced graphene nanoribbon by multiple unit widths of one FMN ribbon. This might explain the multiple widths of the observed graphene nanoribbons. Additionally, the random orientation of the microscopic straight cuts on graphene was ascribed to polycrystalline grain domain assembled by organic molecules on the HOPG surface [36]. These crystallinities may affect the unzipping direction of the template graphene nanoribbon. More evidence for this graphene nanostructure was obtained from Raman spectroscopy.

3.3. Raman characteristics of dispersed graphene

The dispersion was further characterized by Raman spectroscopy, a powerful tool that can be used to provide defect information for graphene. For this, widefield Raman (WFR) spectroscopy [23] with a single bandpass filter (see Methods for the detailed WFR spectroscopies) was utilized. G and 2D band images (Fig. 5A and B) near 1580 and 2680 cm⁻¹,

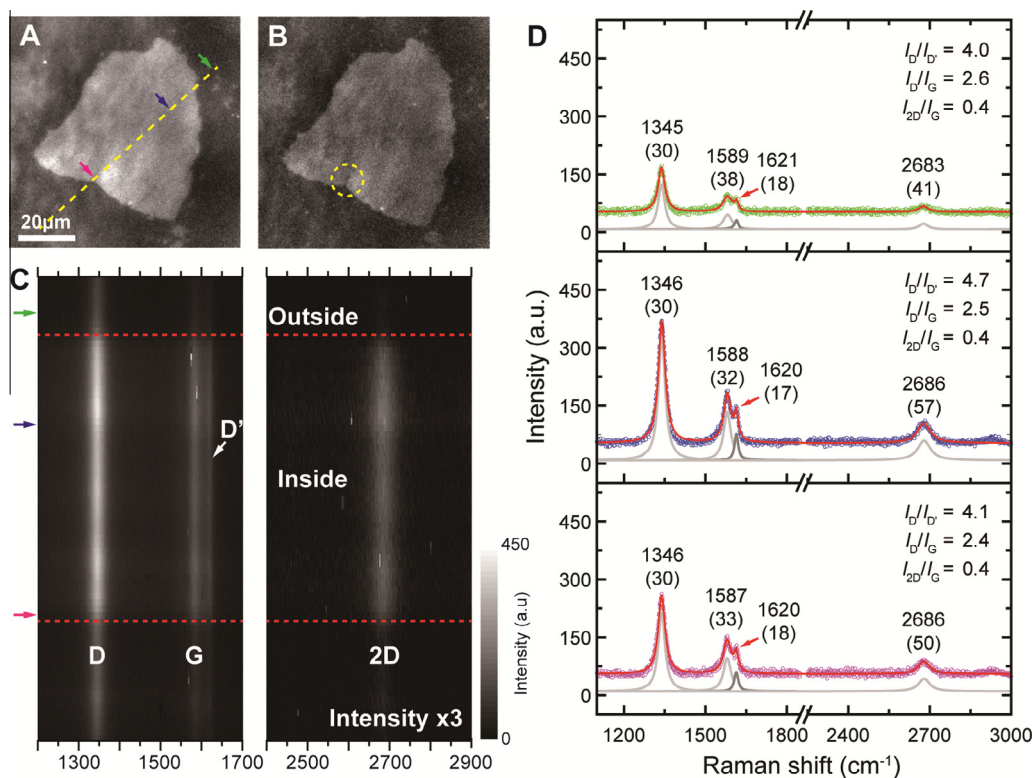


Fig. 5 – Raman images from (A) G and (B) 2D bands. (C) Line Raman spectra from the dashed yellow line of (A). Note that 2D band intensity was multiplied by 3 times. (D) Raman spectra obtained from the color-coded arrows in (A and C). The measured data and summed curve were offset by 45 vertical counts for clarity. The bracket notes FWHM of the Raman bands obtained from deconvolution with Lorentzian line shapes. The excitation wavelength is 532 nm. (A colour version of this figure can be viewed online.)

respectively, clearly illustrate that the G band intensity is much greater than that of the 2D band. As shown in Fig. 5C, the line Raman spectra obtained along the dashed yellow line in Fig. 5A displayed sharp Raman features of graphene (i.e., D, G, D', and 2D bands). Those were observed within the graphene flake (i.e., between red dotted lines), along even outside the flake, although their inside intensities are approximately three times higher than that of outside region. The existence of Raman signals outside the flake is reminiscent of the small unzipped graphene flakes with few hundreds nanometer in length.

The Raman spectra obtained at several points (the color arrows in Fig. 5A and C) are displayed in Fig. 5D. The top (green), and middle and bottom (blue and red) spectra were obtained from outside and inside the graphene flake. The green Raman trace displays a significant D band, with the G, D', and 2D bands presented in order of decreasing intensity. The position of the D band (ω_D) is situated at 1345 cm^{-1} , and the intensity ratio of D over G bands (I_D/I_G) is 2.6, suggesting a high level of defects [37]. In addition, the overlapped G and D' bands, which were resolved by deconvoluting with Lorentzian line shapes as a published literature [38]. The position (ω_G) and FWHM (Γ_G) of the G band are 1589 and 38 cm^{-1} , while those of the D' band are 1621 and 18 cm^{-1} , respectively. The intensity of the 2D band is significantly less than that of the G band, displaying ω_{2D} and Γ_{2D} with 2683 and 41 cm^{-1} ,

respectively. The origin of upfield-shifted G band as compared to that of mechanically exfoliated monolayer graphene (1580 cm^{-1}) [39] originates from disorder-induced heterogeneity [40]. The intensity ratio of D over D' ($I_D/I_{D'}$), D over G (I_D/I_G), and 2D over G bands (I_{2D}/I_G) from each spot are also listed in Fig. 5D. With this information, the defect density, and nature of defects can be estimated [41]. The I_D/I_G ratio can be utilized to express the defect density (L_D , in nm^{-1} average distance between two defects) [41] by using following equation (the modified Tuinstra-Koenig relation),

$$I_D/I_G = C_A \times \pi(r_A^2 - r_S^2)/L_D^2$$

where C_A is the wavelength-dependent parameter, and r_A and r_S are radius of the area surrounding point defect, and of structurally disordered area, respectively [41]. Considering the excitation-dependent parameter, $C_A = 5.4 \pm 1.6 \text{ eV}^{-4}$ at the excitation laser (532 nm), and previously determined r_A and r_S values (i.e., 3.1 and 1 nm) [41], the estimated average distance (L_D) between defects was approximately 7.4 nm, which is nearly two times smaller than that determined by HRTEM study (i.e., 16 nm). This discrepancy may originate from the absence of D band from zigzag-edged nanoribbons [42]. Raman results support the observed lined unzipping of graphene in HRTEM study.

The nature of these defects can be further obtained by investigating the intensity ratio of D over the D' band

($I_D/I_{D'}$). Casiraghi et al. [38] reported that defects can be classified into three natures: sp^3 , vacancy (or hole), and boundary (edge) defects according to the $I_D/I_{D'}$ value. While the sp^3 -type defect had an $I_D/I_{D'}$ of 13, those of the vacancy and boundary defects were 7 and 3.5, respectively. The measured $I_D/I_{D'}$ ratio near 4.0 in the sample indicates the boundary defects. The geometric consideration of graphene with edge defect indicated that only torn graphene with a width of a few nanometers can match this value.

Inside and outside regions of the graphene flake display almost similar Raman vibrational positions varying within 2 cm^{-1} . This indicates that sonication-assisted dispersion provides quite uniform properties throughout graphene flakes. The $I_D/I_{D'}$ ratio varies from 4.0 to 4.7, from outside to inside the graphene flake, suggesting that large graphene flakes have slightly larger vacancy defects. It is noteworthy that cracked part of the graphene flake (circle in Fig. 5B) exhibits intermediate value (i.e., 4.1), supporting that graphene edges with lower the $I_D/I_{D'}$ ratios. Similar $I_D/I_{D'}$ ratios (i.e., 4.2–4.5, inside and outside graphene flakes) were observed from graphene flakes obtained from a separate batch, as shown in Fig. S6 of the SI.

In order to analyze chemical functionalities of graphene films, X-ray photoelectron spectroscopy (XPS) was conducted (see Figs. S7 & S8 of the SI and Methods for detailed explanation). The sp^2 carbon explained nearly 82% of the atomic content, while other bonds, such as sp^3 carbon, C–O of epoxide, and carboxylic acid were present at 12.6%, 3.7%, and 2.0%, respectively. This suggests that carboxylic acids are preferentially decorated on the edge of graphene and GNR, while basal plane of graphene is also decorated with epoxide moiety. This graphene displayed much greater sp^2 content than those of the reduced graphene oxide (RGO) [43], suggesting that the edge of the graphene is possibly terminated by the oxygenated species.

3.4. Electrical properties of graphene films

In order to examine the electrical properties of these graphene dispersions, their sheet resistances of the graphene films (see Methods) were measured according to transmittance, T . Annealing the sample at $300\text{ }^\circ\text{C}$ under air for 2 h prior to measurement greatly improves the electrical performance, similar to the enhanced contrast and reduced height of the aforementioned annealing graphene sample. As a control sample, thick graphene films were prepared with transmittance values of 0.03%. Thermal annealing led to an order-of-magnitude decrease in sheet resistance (i.e., from 1800 to $130\text{ }\Omega/\text{sq}$), indicating that thermal annealing is pivotal to the removal of organic surfactant and improvement of vdW contact between graphene flakes, corroborating the results of the optical experiments. Fig. 6 displays the sheet resistances obtained from graphene films with various transmittances (i.e., 12%, 31%, 65%, and 75%, whose transmittance curves are shown in Fig. S9 of the SI), along with photographs of the corresponding transparent sheets on slide glass. By increasing the transmittance from 12% to 75%, the sheet resistance increased from 0.88 to $28\text{ k}\Omega/\text{sq}$, respectively. If the logarithmic scaling of the transmittance to the film thickness is considered, the contact resistance between the

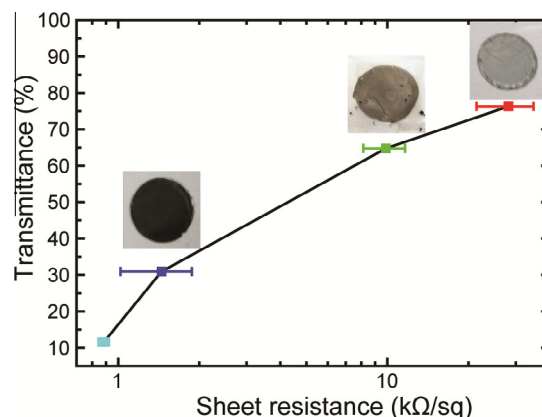


Fig. 6 – Sheet resistances of the graphene films with various transmittances (i.e., 12%, 31%, 65%, and 75%), measured by a four-probe current–voltage measurement. Lines are drawn for a visual guide. The inset displays the prepared graphene films on slide glass. (A colour version of this figure can be viewed online.)

graphene flake played a role in the overall sheet resistance of the produced graphene film. Although this value is an order of magnitude greater than that of single-layered CVD graphene (i.e., $125\text{ }\Omega/\text{sq}$ from 97.4% T) [44], this value is better than that of RGO (i.e., $200\text{ k}\Omega/\text{sq}$ from 75% T) [43] and is comparable to that from sodium cholate-exfoliated graphene (i.e., $20\text{ k}\Omega/\text{sq}$ from 75% T) [24]. This demonstrates the excellent electrical characteristics of the dispersed graphene with solution processability.

In order to confirm whether these graphene films have field-effect transistor (FET) characteristics, transistors with a bottom gate were fabricated using a metal mask on top of the graphene. Fig. S10A and its inset of the SI display OM images of the fabricated device, whose channel length is approximately $50\text{ }\mu\text{m}$, on top of transferred graphene film with 94% T, which corresponds to bilayer graphene. With this graphene film, FET performance varies according to devices presumably due to unevenly distributed graphene film. The current–voltage (I – V) plot (Fig. S10B) displays that blue and red plot displays a slight sigmoidal curves in the meanwhile purple and red plots exhibits nearly straight line, suggesting that thin graphene film slightly deviate its metallic behavior. The low gate response of I_D according to sweeping V_G (Fig. S10C of the SI) might originate from either the continuous graphene flake along two electrodes or a small portion of graphene nanoribbons because metallic constituent governs device performance. Sorting GNR from the bulk graphene samples using density gradient ultracentrifugation [24] would be helpful to elucidate its structure–property relationship, which will be future topic.

4. Conclusion

Readily-available FMN and its analogue were able to produce graphene nanoribbons dispersion. HRTEM revealed that graphene dispersion contains straight-edged graphene nanoribbons smaller than a few tens of nanometers in width and few hundreds nanometer in length. GNR formation was

ascribed to the template effect of one-dimensional organization of FMN on a graphene surface, providing self-assembled unzipping template upon sonication. Raman study revealed that graphene flakes containing GNR and cut displayed large D and D' peaks, supporting the observed edge defect. Bulk graphene film displayed low resistance as well. This study provided a facile method for producing large quantities of graphene nanoribbons with sub-10-nm width in solution for future applications in high-performance transistors, spintronics, and membrane materials.

5. Conflict of interest

The authors declare no conflict of interest.

Acknowledgements

The authors thank H. Oh for initial help. This research was supported by the Basic Science Research Program through the National Research Foundation of Korea (NRF), funded by the Ministry of Education, Science and Technology (NRF-2011-0015154), and supported in part by Yonsei University Future-Leading Research Initiative 2014.

Appendix A. Supplementary data

Supplementary data associated with this article can be found, in the online version, at <http://dx.doi.org/10.1016/j.carbon.2014.09.097>.

REFERENCES

- [1] Dössel L, Gherghel L, Feng X, Müllen K. Graphene nanoribbons by chemists: nanometer-sized, soluble, and defect-free. *Angew Chem Int Ed* 2011;50(11):2540–3.
- [2] Wang X, Ouyang Y, Li X, Wang H, Guo J, Dai H. Room-temperature all-semiconducting sub-10-nm graphene nanoribbon field-effect transistors. *Phys Rev Lett* 2008;100(20):206803.
- [3] Son Y-W, Cohen ML, Louie SG. Energy gaps in graphene nanoribbons. *Phys Rev Lett* 2006;97(21):216803.
- [4] Li X, Wang X, Zhang L, Lee S, Dai H. Chemically derived ultrasmooth graphene nanoribbon semiconductors. *Science* 2008;319(5867):1229–32.
- [5] Nakada K, Fujita M, Dresselhaus G, Dresselhaus MS. Edge state in graphene ribbons: nanometer size effect and edge shape dependence. *Phys Rev B* 1996;54(24):17954–61.
- [6] Wakabayashi K, Fujita M, Ajiki H, Sigrist M. Electronic and magnetic properties of nanographite ribbons. *Phys Rev B* 1999;59(12):8271–82.
- [7] Campos LC, Manfrinato VR, Sanchez-Yamagishi JD, Kong J, Jarillo-Herrero P. Anisotropic etching and nanoribbon formation in single-layer graphene. *Nano Lett* 2009;9(7):2600–4.
- [8] Datta SS, Strachan DR, Khamis SM, Johnson ATC. Crystallographic etching of few-layer graphene. *Nano Lett* 2008;8(7):1912–5.
- [9] Ci L, Xu Z, Wang L, Gao W, Ding F, Kelly K, et al. Controlled nanocutting of graphene. *Nano Res* 2008;1(2):116–22.
- [10] Kosynkin DV, Higginbotham AL, Sinitskii A, Lomeda JR, Dimiev A, Price BK, et al. Longitudinal unzipping of carbon nanotubes to form graphene nanoribbons. *Nature* 2009;458(7240):872–6.
- [11] Jiao L, Wang X, Diankov G, Wang H, Dai H. Facile synthesis of high-quality graphene nanoribbons. *Nat Nanotechnol* 2010;5(5):321–5.
- [12] Jiao L, Zhang L, Wang X, Diankov G, Dai H. Narrow graphene nanoribbons from carbon nanotubes. *Nature* 2009;458(7240):877–80.
- [13] Han MY, Özyilmaz B, Zhang Y, Kim P. Energy band-gap engineering of graphene nanoribbons. *Phys Rev Lett* 2007;98(20):206805.
- [14] Cai J, Ruffieux P, Jaafar R, Bieri M, Braun T, Blankenburg S, et al. Atomically precise bottom-up fabrication of graphene nanoribbons. *Nature* 2010;466(7305):470–3.
- [15] Liu Z, Liu JZ, Cheng Y, Li Z, Wang L, Zheng Q. Interlayer binding energy of graphite: a mesoscopic determination from deformation. *Phys Rev B* 2012;85(20):205418–22.
- [16] Ju S-Y, Kopcha WP, Papadimitrakopoulos F. Brightly fluorescent single-walled carbon nanotubes via an oxygen-excluding surfactant organization. *Science* 2009;323(5919):1319–23.
- [17] Long B, Manning M, Burke M, Szafranek BN, Visimberga G, Thompson D, et al. Non-covalent functionalization of graphene using self-assembly of alkane-amines. *Adv Funct Mater* 2012;22(4):717–25.
- [18] Ferrari AC, Basko DM. Raman spectroscopy as a versatile tool for studying the properties of graphene. *Nat Nanotechnol* 2013;8(4):235–46.
- [19] Blake P, Hill EW, Castro Neto AH, Novoselov KS, Jiang D, Yang R, et al. Making graphene visible. *Appl Phys Lett* 2007;91(6):063124.
- [20] Ni ZH, Wang HM, Kasim J, Fan HM, Yu T, Wu YH, et al. Graphene thickness determination using reflection and contrast spectroscopy. *Nano Lett* 2007;7(9):2758–63.
- [21] Sim J, Oh H, Koo E, Ju S-Y. Effect of tight flavin mononucleotide wrapping and its binding affinity on carbon nanotube covalent reactivities. *Phys Chem Chem Phys* 2013;15(44):19169–79.
- [22] Ju S-Y, Doll J, Sharma I, Papadimitrakopoulos F. Selection of carbon nanotubes with specific chiralities using helical assemblies of flavin mononucleotide. *Nat Nanotechnol* 2008;3(6):356–62.
- [23] Havener RW, Ju S-Y, Brown L, Wang Z, Wojcik M, Ruiz-Vargas CS, et al. High-throughput graphene imaging on arbitrary substrates with widefield Raman spectroscopy. *ACS Nano* 2011;6(1):373–80.
- [24] Green AA, Hersam MC. Solution phase production of graphene with controlled thickness via density differentiation. *Nano Lett* 2009;9(12):4031–6.
- [25] Kamiya K, Hashimoto K, Nakanishi S. Instantaneous one-pot synthesis of Fe-N-modified graphene as an efficient electrocatalyst for the oxygen reduction reaction in acidic solutions. *Chem Commun* 2012;48(82):10213–5.
- [26] Gaboardi M, Bliersbach A, Bertoni G, Aramini M, Vlahopoulou G, Pontiroli D, et al. Decoration of graphene with nickel nanoparticles: study of the interaction with hydrogen. *J Mater Chem A* 2014;2(4):1039–46.
- [27] Lin CS, Zhang RQ, Niehaus TA, Frauenheim T. Geometric and electronic structures of carbon nanotubes adsorbed with flavin adenine dinucleotide: a theoretical study. *J Phys Chem C* 2007;111(11):4069–73.
- [28] Gao Z, Zhi C, Bando Y, Golberg D, Serizawa T. Noncovalent functionalization of disentangled boron nitride nanotubes with flavin mononucleotides for strong and stable visible-light emission in aqueous solution. *ACS Appl Mater Inter* 2011;3(3):627–32.

- [29] McCreery RL. In: Winefordner JD, editor. *Raman Spectroscopy for Chemical Analysis*. New York: John Wiley & Sons Inc; 2000. p. 1–2.
- [30] Nair RR, Blake P, Grigorenko AN, Novoselov KS, Booth TJ, Stauber T, et al. Fine structure constant defines visual transparency of graphene. *Science* 2008;320(5881):1308.
- [31] Hernandez Y, Nicolosi V, Lotya M, Blighe FM, Sun Z, De S, et al. High-yield production of graphene by liquid-phase exfoliation of graphite. *Nat Nanotechnol* 2008;3(9):563–8.
- [32] Bets K, Yakobson B. Spontaneous twist and intrinsic instabilities of pristine graphene nanoribbons. *Nano Res* 2009;2(2):161–6.
- [33] Shenoy VB, Reddy CD, Ramasubramaniam A, Zhang YW. Edge-stress-induced warping of graphene sheets and nanoribbons. *Phys Rev Lett* 2008;101(24):245501.
- [34] Zhang J, Chi Q, Wang E, Dong S. A comparative study on STM imaging and electrocatalytic activity of different surfaces modified with flavin adenine dinucleotide. *Electrochim Acta* 1995;40(6):733–44.
- [35] Ju S-Y, Abanulo DC, Badalucco CA, Gascón JA, Papadimitrakopoulos F. Handedness enantioselection of carbon nanotubes using helical assemblies of flavin mononucleotide. *J Am Chem Soc* 2012;134(32):13196–9.
- [36] Tao F, Bernasek SL. Understanding odd–even effects in organic self-assembled monolayers. *Chem Rev* 2007;107(5):1408–53.
- [37] Lucchese MM, Stavale F, Ferreira EHM, Vilani C, Moutinho MVO, Capaz RB, et al. Quantifying ion-induced defects and Raman relaxation length in graphene. *Carbon* 2010;48(5):1592–7.
- [38] Eckmann A, Felten A, Mishchenko A, Britnell L, Krupke R, Novoselov KS, et al. Probing the nature of defects in graphene by Raman spectroscopy. *Nano Lett* 2012;12(8):3925–30.
- [39] Ferrari AC, Meyer JC, Scardaci V, Casiraghi C, Lazzeri M, Mauri F, et al. Raman spectrum of graphene and graphene layers. *Phys Rev Lett* 2006;97(18):187401.
- [40] Krauss B, Lohmann T, Chae DH, Haluska M, von Klitzing K, Smet JH. Laser-induced disassembly of a graphene single crystal into a nanocrystalline network. *Phys Rev B* 2009;79(16):165428.
- [41] Cancado LG, Jorio A, Ferreira EH, Stavale F, Achete CA, Capaz RB, et al. Quantifying defects in graphene via Raman spectroscopy at different excitation energies. *Nano Lett* 2011;11(8):3190–6.
- [42] Cancado LG, Pimenta MA, Neves BRA, Dantas MSS, Jorio A. Influence of the atomic structure on the Raman spectra of graphite edges. *Phys Rev Lett* 2004;93(24):247401.
- [43] Eda G, Fanchini G, Chhowalla M. Large-area ultrathin films of reduced graphene oxide as a transparent and flexible electronic material. *Nat Nanotechnol* 2008;3(5):270–4.
- [44] Bae S, Kim H, Lee Y, Xu XF, Park JS, Zheng Y, et al. Roll-to-roll production of 30-inch graphene films for transparent electrodes. *Nat Nanotechnol* 2010;5(8):574–8.

Graphene Nanoribbons Formed by a Sonochemical Graphene Unzipping using Flavin Mononucleotide as a Template

Woojin Yoon¹, Yonggeun Lee¹, Hongje Jang¹, Myungsoo Jang¹, Jin Sung Kim², Hee Sung Lee², Seongil Im², Doo Wan Boo¹, Jiwoong Park³, and Sang-Yong Ju^{1,}*

¹Department of Chemistry, Yonsei University, Seoul 120-749, Republic of Korea,

²Department of Physics, Yonsei University, Seoul 120-749, Republic of Korea, and

³Department of Chemistry and Chemical Biology, Cornell University, Ithaca, New York 14853, USA

* Correspondence E-mail: syju@yonsei.ac.kr

1. Contact angle measurement

Contact angle measurement of the amine-modified substrate was conducted using a custom-made setup with a blunt-tip HPLC syringe (25 μL , Hamilton). A 5 μL aliquot was dropped on the substrates and the drop shape was recorded using the CMOS CCD camera. This process was repeated five times to obtain an average contact angle. The contact angle with the substrate was further analyzed using an ImageJ program with a Low-Bond Axisymmetric Drop Shape Analysis (LBADSA) plug-in.

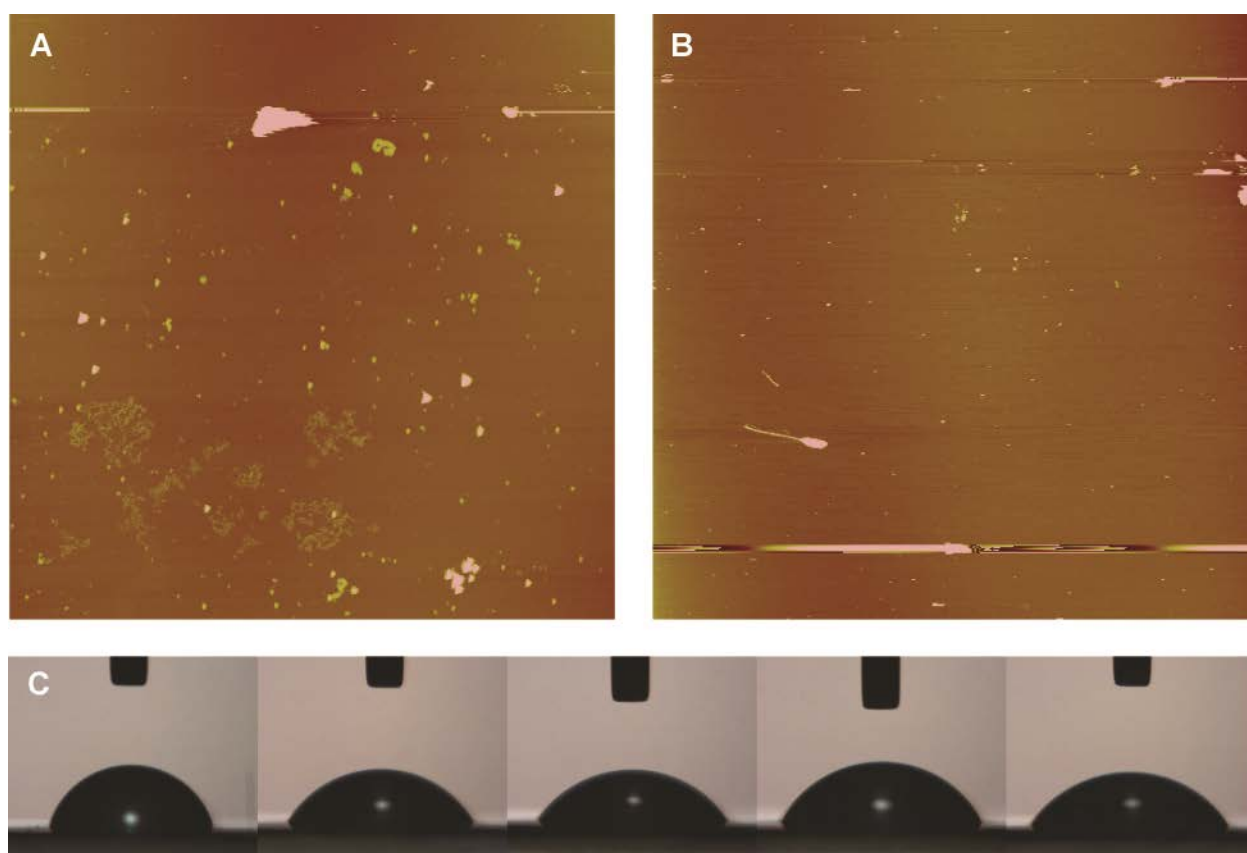


Figure S1. AFM images of (A) APTES- and (B) APDMES-functionalized, 285-nm thick SiO_2/Si substrates. (C) Contact angle measurement of the APDMES-functionalized substrate, whose average contact angle was $63.2^\circ \pm 7.0$.

2. Annealing effect on deposited graphene

OM images (Figure S2A) and the resulting optical contrast along the graphene flake (red trace in Figure S1A) were measured by a monochromatic CCD detector (see the Methods for the detailed measurement) with 550 nm bandpass filter to the excitation side. The size of this graphene flake was $\sim 60 \mu\text{m}$ in the lateral length. The subsequent contrast was calculated using following equation (the contrast equation),

$$C = (R - R_o) / R_o \quad (\text{S1})$$

where C is the contrast and R and R_o are reflectances obtained from the graphene/substrate and substrate only, respectively.^[S1] The resulting contrast value was 0.13 along the yellow dashed line in Figure S2A, which is greater than that of the single-layered graphene (*i.e.*, 0.9).^[S1] In order to verify the effect of probable intercalated surfactants between graphene layers, the corresponding optical and AFM images were re-acquired from the same sample after annealing at 300 °C for 2 hrs, as shown in Figure S2C and D. First, the contrast values increased to 0.14 upon annealing, as shown in Figure S2C, suggesting that annealing eliminates interstitial FMNs and enhances vdW interactions between the graphene layers. The contrast image after annealing (Figure S2C) displays a relaxed contrast and many graphene crumbs less than 1 μm in length. The graphene crumbs were highly visible after thermal annealing, adding proof that thermal annealing effectively enhances vdW interaction between graphene flakes.

The corresponding AFM topographies displayed several differences upon annealing (Figure S2B and D). The resulting overall height profiles after Ar annealing decreased from 3.4 to 1.9 nm. An approximate 1.5-nm height difference seems to originate from the removal of trapped surfactants, along with better vdW interactions between graphene layers since high temperature annealing assists graphene in conforming to the underlying topography.^[S2] This height value suggests that the number of graphene layers is less than 5. In addition, the root mean square (RMS) roughness of the graphene surface increased from 3.3 to 6.3 nm (see increased spike-like feature above the plane of height profile in Figure

S1D as compared to S1B). The RMS roughness (*i.e.*, 2.0 nm) of the amine-terminated substrate suggests that the high-temperature-resistant graphene crumbs introduced protruding features.

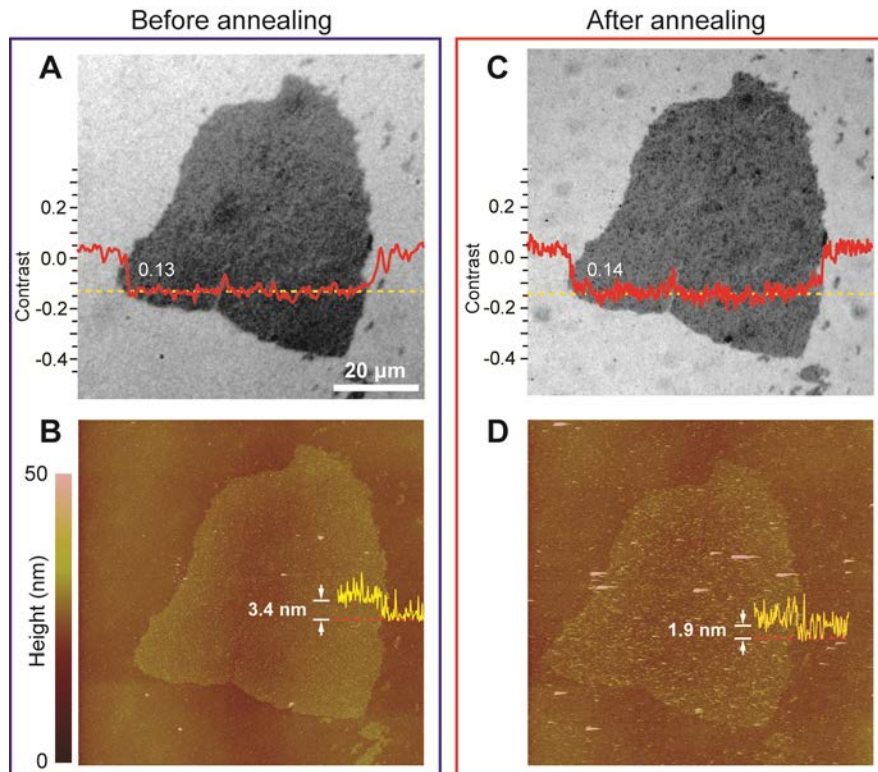


Figure S2. Annealing effect of a few-layered graphene deposited on a 285-nm SiO₂/Si substrate. (A and B) (A) Optical contrast image, and (B) AFM height images of the corresponding graphene flake prior to Ar annealing at 300 °C. Red traces in (A) and (C) indicate the optical contrast value along the yellow dashed line. Yellow traces indicate the height profile along the red dashed line. (C) Optical contrast image, and (D) AFM height images obtained after annealing.

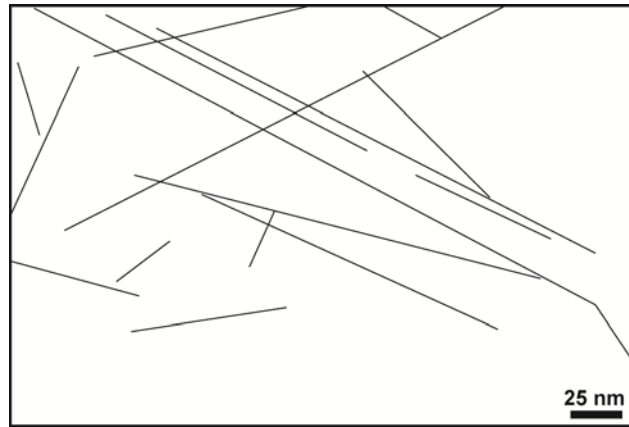


Figure S3. Calculation of defect densities on the graphene flake by HRTEM. Explicit illustration of cutting lines on graphene in Figure 3B. The total length of the lines and area were 1942 nm and 61459 nm², respectively.

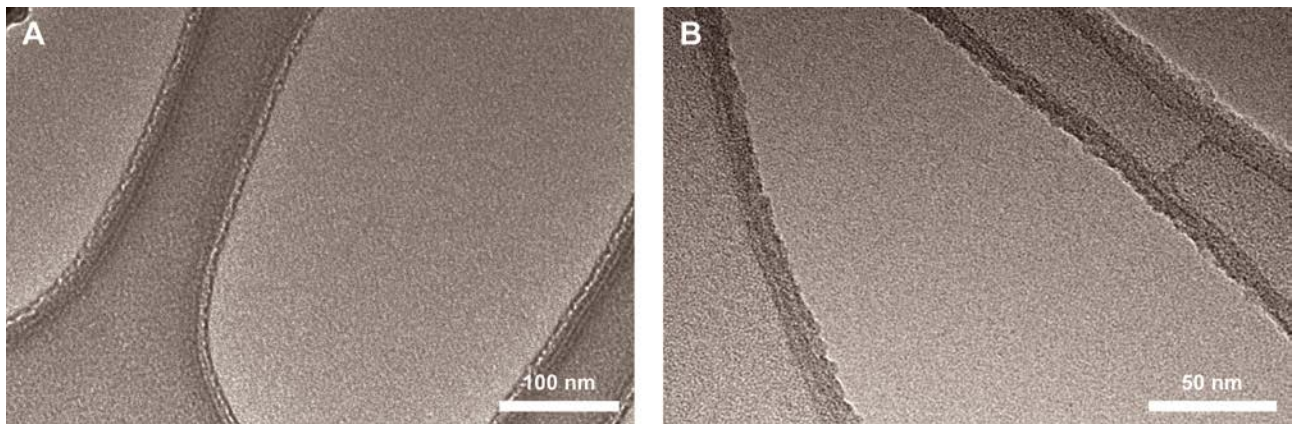


Figure S4. Control experiment of bare grid treated 5 sec oxygen plasma.

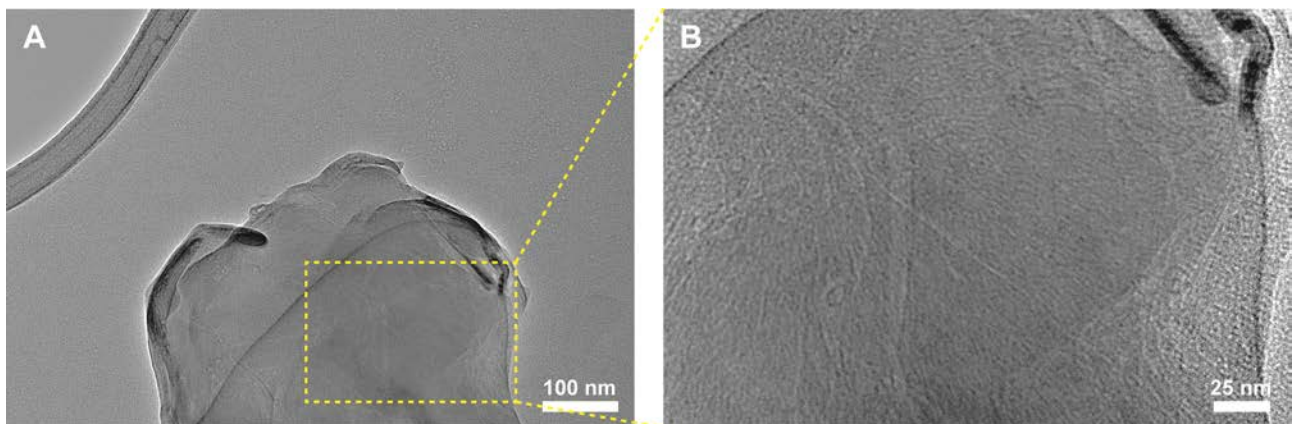


Figure S5. HRTEM images of sodium dodecyl sulfate (SDS)-assisted graphene dispersion.

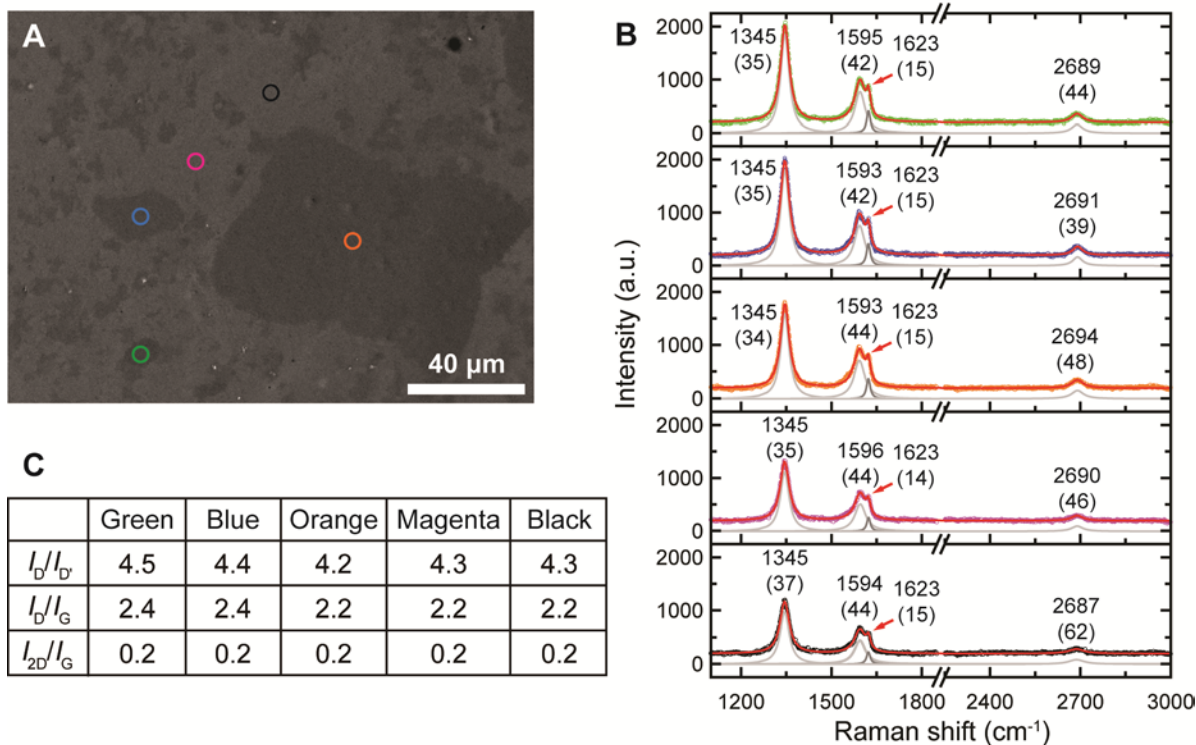


Figure S6. Additional Raman spectra of graphene flakes from a different batch. (A) OM image of deposited graphene flakes. (B) Raman spectra and their band positions obtained from various positions of (A). (C) The corresponding I_D/I_D' , I_D/I_G , and I_{2D}/I_G ratios of Raman traces.

3. XPS analysis

X-ray photoelectron spectroscopy (XPS) was conducted to analyze the atomic content of graphene sheets. First, the substrates were subjected to a survey scan, as shown in Figure S7. Detailed scans of the C1s core from the FMN-derived graphene sample after annealing are shown in Figure S8. In order to pinpoint the bonding information, the spectra were further deconvoluted to six peaks: the related bonding nature (its center positions) of carbon sp^2 (C=C, 284.5 eV), carbon sp^3 (C-C, 285.1 eV), amine (C-N, 285.7 eV), epoxy/hydroxyl (C-O/C-OH, 286.2-286.8 eV), carbonyl (C=O, 287.1-287.3 eV), and carboxylates (O-C=O, 288.3-289.1 eV). Since nitrogen contribution can be obtained only from residual FMN, its contribution was subtracted (Table S1 lists their positions and relative areas). While graphene

dispersions displayed prominent C1s, the O1s peaks and the remaining peaks, such as N1s and Si2p, and Na1s, exhibited different concentrations. Since we utilized soda-lime slide glass and a SiO₂/Si substrate for the measurement, the contributions of Na and Si were eliminated, which supports the qualitative information on atomic content. The atomic percentages of the elements are represented in Table S1. N1s and Si2p peaks originated from surfactants and substrates for XPS measurements; ~4% of the carbon 1s peak is due to carbons in FMN.

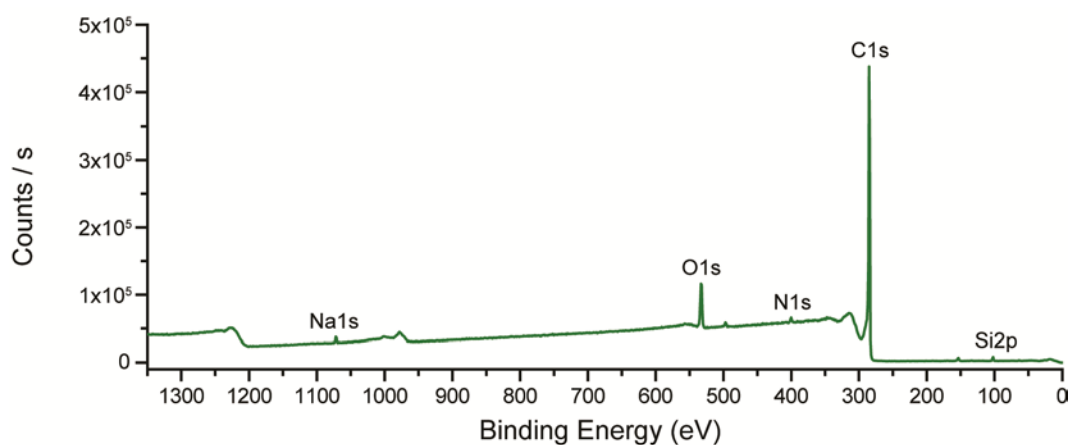


Figure S7. XPS survey scans of the FMN-derived graphene samples.

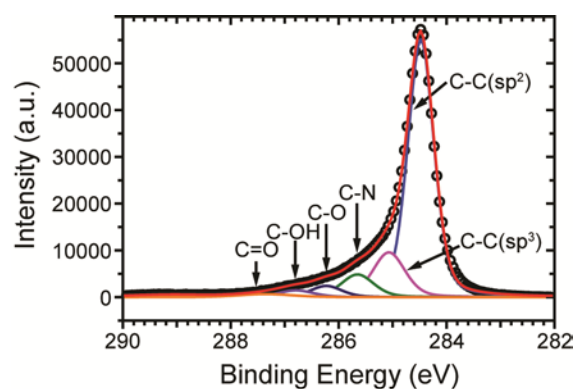
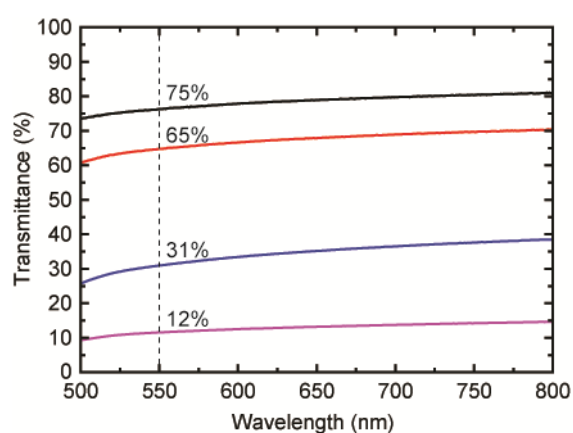
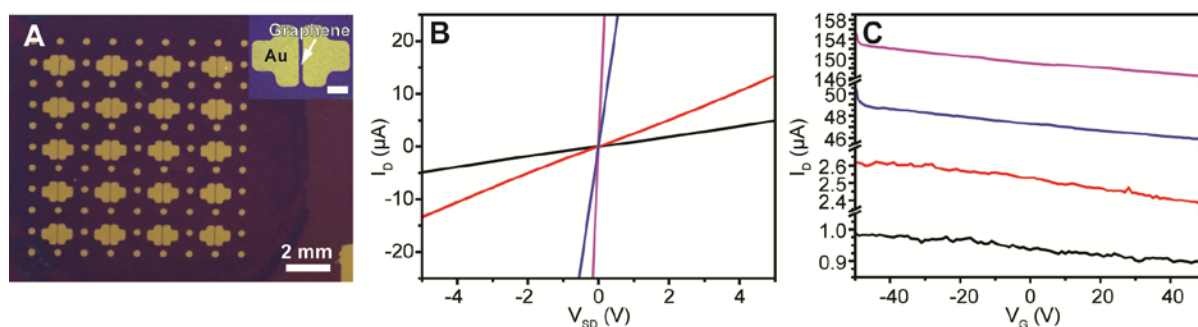


Figure S8. Carbon 1s core-level XPS from the FMN-removed graphene film. The Shirley background was subtracted for clarity. The original data was displayed in a circle while the summed graph of the deconvoluted peak is shown in the red curve.

Table S1. Bonding information of the FMN-dispersed graphene dispersion obtained from XPS

Bonding species	Binding energy (eV)	Relative area (%)	Subtraction of contribution from surfactant →	Bonding species	Relative area (%)
C-C (sp ²)	284.5	68.2		C-C (sp ²)	81.7
C-C (sp ³)	285.1	14.5		C-C (sp ³)	12.6
C-N	285.7	7.5		C-O	3.7
C-O	286.2	3.6		C=O	0.0
C-OH	286.8	2.4		carboxyl	2.0
C=O	287.4	1.7			
Carboxyl	289.1	1.5			

**Figure S9.** Transmittance curves with varying graphene film thickness.**Figure S10.** Bottom-gated field effect transistor (FET) using annealed graphene film with 100-nm-thick gold electrodes. (A) OM image of FET devices array. Inset displays individual device. Scale bar of inset: 300 μm . (B) Current-voltage (I-V) curves of graphene films of 94% transmittances. Each color represents different devices. The channel length and width are approximately 50 and 750 μm , respectively. (C) Gate voltage characteristics using $V_{SD}= 1\text{ V}$.

Cited references

- [S1] P. Blake, E. W. Hill, A. H. Castro Neto, K. S. Novoselov, D. Jiang, R. Yang, T. J. Booth, A. K. Geim, *Appl. Phys. Lett.* **2007**, *91*, 063124.
- [S2] F. Tao, S. L. Bernasek, *Chem. Rev.* **2007**, *107*, 1408.